Unsteady CFD Analysis of Alternating Flow Patterns in a Restrictive Orifice of a Pressure Regulator Valve

Naoki Hirose[1], Seiei Masuda[1], Yasushi Matsunaga[1], Fumio Shimizu[2], Kazuhiro Tanaka[2], Takeshi Yamaguchi[2]

[1] *IHI Corporation, Control Systems Engineering Department, 3-2-1 Daikanyama, Akishima City, Tokyo, Japan**

[2] *Kyushu Institute of Technology, Graduate School of Computer Science and Systems Engineering, 680-4 Kawazu, Iizuka-city, Fukuoka, JAPAN***

E-mail: hirose3694@ihi-g.com; masuda4361@ihi-g.com; matsunaga4536@ihi-g.com; shimizu@phys.kyutech.ac.jp; tanakafa@fka.att.ne.jp; aw.fluidlab@gmail.com

Abstract.

The damping force generated by the damping orifice installed in a pressure-regulating valve is regarded as a key factor governing the overall stability and dynamic response of the valve. However, this damping force varies in a complex manner depending on the local flow field around the orifice, the amplitude of the volumetric flow rate, and the excitation frequency, and its fundamental mechanisms have not yet been fully clarified. To elucidate these mechanisms, three-dimensional unsteady CFD analyses were performed for the flow around the damping orifice within a pressure-regulating valve system, and the resulting flow patterns were examined in detail. The analyses revealed that, under unidirectional-flow conditions, a highly unsteady vortical structure is formed in which starting and stopping vortices are generated and subsequently collapse, whereas under alternating-flow conditions, distinctly different flow fields appear on the upstream and downstream sides of the orifice. This paper reports on these characteristic flow-field structures.

Keywords. Pressure Control Valve, Damping Orifice, Alternative Flow, Flow Pattern, CFD

1. INTRODUCTION

The configuration of the pressure regulator system is shown in Figure 1.1. In the pressure regulator valve, which operates with the pre-compression of the feedback spring as the input and regulates the outlet pressure to remain constant against variations in flow demand, the damping force generated by the damping orifice is extremely important for ensuring system stability. The system damping directly changes the phase margin of the valve spring–mass dynamics; increasing the damping force enlarges the phase margin and thereby enhances stability. On the other hand, excessive damping causes velocity saturation of the valve. Once the valve motion is velocity-saturated, its dynamic response becomes insufficient over the operating range, and therefore the trade-off between stability and responsiveness becomes critical. Research on orifice flows has a long history, particularly regarding discharge coefficients under steady-flow conditions [1]. Subsequently, transient flow and system dynamics in piping systems without orifices have been investigated [2,3], and macroscopic studies have also been conducted for piping systems that include orifices [4]. In Reference [4], the dynamic characteristics of orifices are reported in detail, and it is concluded that,

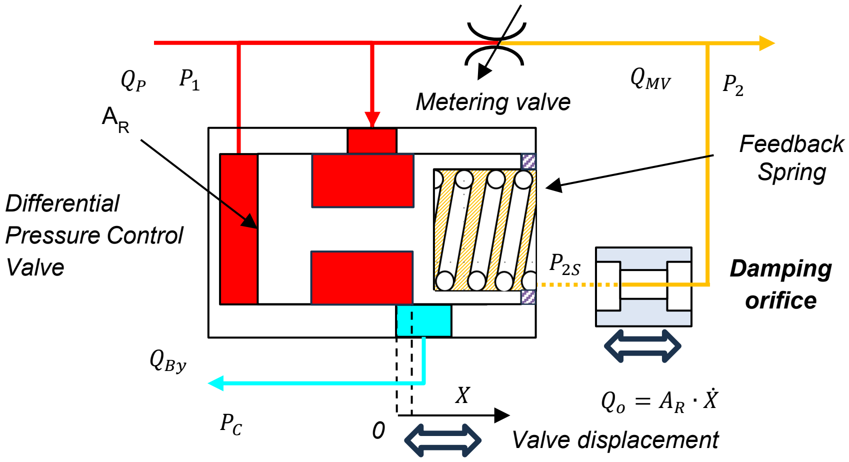

Figure 1.1 Schematic Diagram of a Pressure Regulator Valve

for excitation frequencies below 1000 [Hz], unsteadiness has no significant influence on the flow characteristics. In addition, there are interesting studies that attempt to derive the fluid inertia associated with constrictions in piping [5]. Because inertial and resistive effects of the fluid occur simultaneously and are difficult to separate, further work has combined CFD results with lumped-parameter model to extract the inertial contribution of the orifice section [6]. From a more microscopic standpoint, wall-friction losses in pulsating flows have been examined [7,8], but no study has addressed the combined effect of pulsating flow and an orifice. In view of the above, very few studies have investigated the frequency response and flow patterns of damping orifices as they appear in pressure regulator systems. Masuda et al. [9] compared unsteady CFD results with a one-dimensional bond-graph model [10] and showed that the damping characteristics of an orifice subjected to alternating flow can be represented by a second-order lag system with an additional first-order lead element, and that the resonance frequency decreases relative to the value predicted by the 1D model. They further predicted [11] that this reduction in resonance frequency is caused by two mechanisms: (i) added mass that is carried together with the fluid column in the orifice bore, and (ii) a pulsating jet that temporarily blocks the inlet and outlet of the orifice under alternating-flow conditions, deflecting the flow by 90° from the axial to the radial direction and thereby forming a flow field analogous to the curtain area in a nozzle–flapper mechanism, which enhances the inertial effect. However, their paper does not discuss in detail the relationship between excitation frequency and the associated flow patterns. Oshima et al. [12] and Miyashita [13] reported experimental results on the frequency response of damping orifices but did not address the internal or external flow structures. Loudon et al. [14] analytically solved the unsteady Navier–Stokes equations for one-dimensional laminar flow between parallel plates driven by a sinusoidal pressure gradient and examined in detail the dependence of the velocity profile, volumetric flow rate, and wall shear stress on the Womersley number [15], including changes in profile shape, amplitude, and phase lag. They demonstrated that, similar to circular pipe flow, quasi-steady behaviour occurs for $Wo < 1$, whereas phase lag and distortion of the velocity profile occur for $Wo > 1$. However, their analysis does not consider the flow patterns upstream and downstream of an orifice in unsteady flow. Figure 1.2 shows the flow visualization results obtained by Pullin et al. [16].

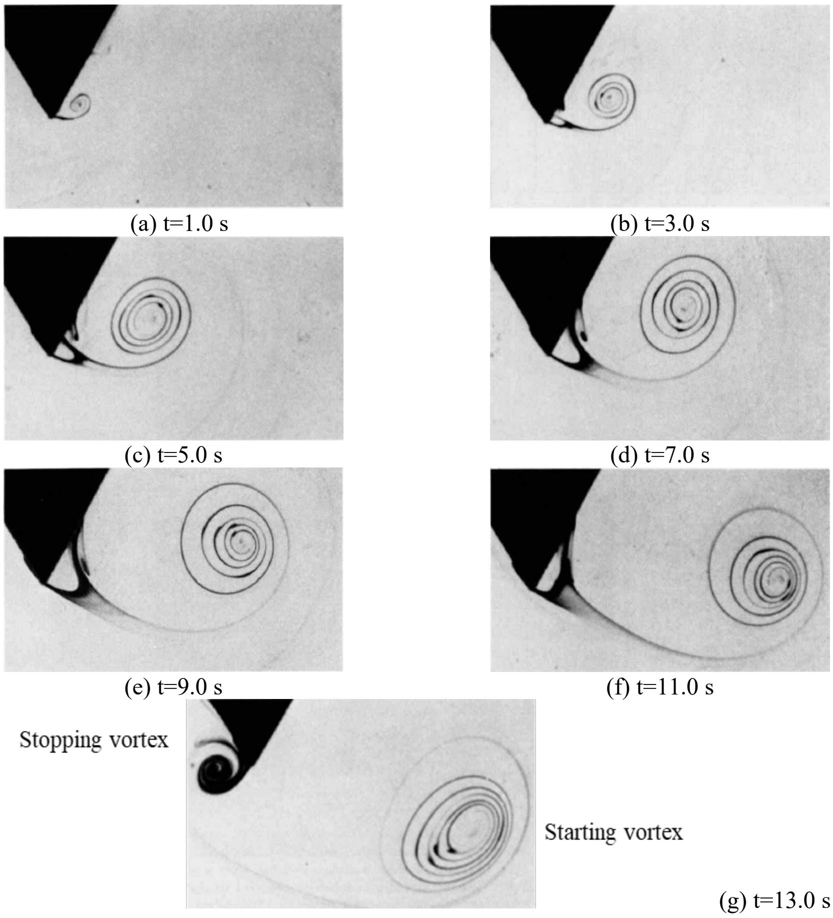

(a) t=1.0 s (b) t=3.0 s (c) t=5.0 s (d) t=7.0 s (e) t=9.0 s (f) t=11.0 s (g) t=13.0 s

Figure 1.2 Starting & Stopping vortex on a wedge photographed by Pullin & Perry [16]

In this study, with the aim of examining and validating the hypothesis proposed by Masuda et al. [9,11] concerning inertial effects in alternating orifice flow, three-dimensional unsteady CFD simulations are performed for the flow around the damping orifice of a pressure regulator valve. The resulting flow structures in the vicinity of the orifice under forward-flow and alternating-flow conditions are investigated in detail and compared with the flow-visualization results of Pullin et al. [16]. Pullin et al. [16] used dye visualization to observe in detail the starting and stopping vortices generated at the leading edge of a 30° wedge and reported the formation process and temporal evolution of the vortex structures associated with the onset and cessation of the flow.

2. NUMERICAL MODELS & CONDITIONS

In this study, three-dimensional unsteady CFD analyses were conducted for the flow field around the damping orifice used in a pressure regulator system, under forward-flow and alternating-flow conditions. This section describes the geometrical configuration of the computational models and the corresponding simulation conditions.

2.1 Numerical calculation conditions

All numerical simulations were performed using Ansys CFX [17] in unsteady mode. A schematic of the computational domain is shown in Figure 2.1. A circular orifice with an inner diameter of 0.62[mm] and a length of 0.7[mm] was placed at the canter of a circular pipe, and straight pipe sections of 25[mm] were provided upstream and downstream of the orifice. This configuration ensures that a fully developed flow reaches the orifice without being affected by the inlet and outlet boundary conditions. The computational grid was locally refined in the vicinity of the orifice and within the downstream shear-layer development region, resulting in a total of approximately 5 million cells. Further details are given in Section 2.4. The simulation conditions are summarized in Table 2.1. A specified volumetric flow rate was imposed at the inlet boundary, a constant-pressure condition was applied at the outlet, and no-slip conditions were enforced on all pipe and orifice walls. The Reynolds number, defined using the orifice diameter as the characteristic length and the maximum flow velocity among the analysed cases, was Re = 290; therefore, all simulations were carried out under laminar-flow assumptions.

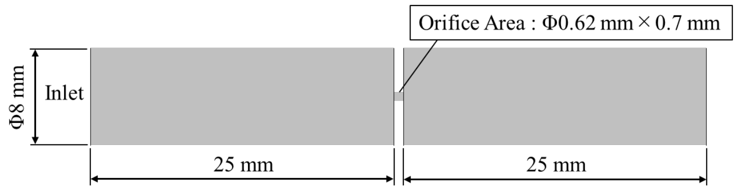

Figure 2.1 3D model of the orifice

Table 2.1 Analysis conditions (general)

Software used	Ansys® CFX [17]
Analysis type	Transient
Turbulence model	Laminar
Fluid density [kg/m^3]	750
Fluid kinematic viscosity [m^2/s]	9.5×10^{-7}
Grid number [-]	5,000,000

2.2 Unidirectional Flow

The computational conditions for the forward-flow case are summarized in Table 2.2 At the inlet, a stepwise variation of the mass flow rate, as shown in Figure 2.2, was imposed. Specifically, a constant mass flow rate of 0.0001 kg/s was prescribed for $0 \leq t < 0.01$ [s]; the mass flow rate was set to zero 0 [kg/s] for $0.01 \leq t < 0.03$ [s]; a constant mass flow rate of 0.0001[kg/s] was again imposed for $0.03 \leq t < 0.05$ [s]; and the mass flow rate was set to zero for $0.05 \leq t < 0.06$ [s]. This configuration enables observation of the periodic vortex shedding and the formation process of stopping vortices that occur when the flow rate is abruptly reduced from a steady forward-flow condition.

Table 2.2 Analysis condition (unidirectional flow)

Inlet flowrate as boundary condition [kg/s] Flow rate:0.0001 [kg/s]： (t=0-0.01, 0.03-0.05 [s]), Flow rate:0 [kg/s]： (t=0.01-0.03, 0.05-0.06 [s])	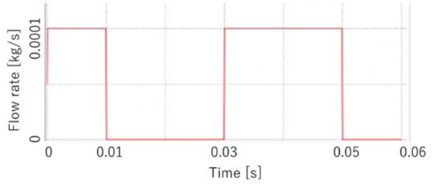 Figure 2.2 Inlet flowrate in unidirectional flow
Outlet boundary condition [MPa]	4

2.3 *Alternative Flow*

The computational conditions for the alternating-flow case are summarized in Table 2.3. At the inlet, an alternating volumetric-flow boundary condition was imposed as shown in Figure 2.3, by applying a sinusoidal velocity with an amplitude of a = 0.0021[m/s] to generate alternating flow. In this study, two excitation frequencies, 200 [Hz] and 1500 [Hz], were considered, and the frequency dependence of the resulting flow field was evaluated for each case. A constant outlet pressure of 4.2 [MPa] was prescribed as the downstream boundary condition. The time step was chosen such that enough time steps per period was secured for each frequency condition. Calculations were performed over several periods, and data obtained after the flow field had reached a periodically steady state were used for the analysis.

Table 2.3 Analysis condition (alternating flow)

Inlet boundary condition [m^3/s] Amplitude; a=0.0021 [m/s] Frequency; f=200, 1500 [Hz] Time variation of displacement; $\dot{X} = a\sin(2\pi f t)$ (1) Cross section area of boundary; A Flow rate $Q = A\dot{X}$ (2)	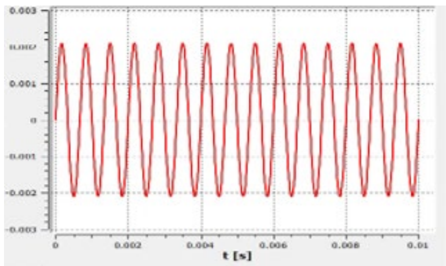 Figure 2.3 Inlet flowrate in alternating flow
Outlet boundary condition [MPa]	4.2

2.4 *Grid independence verification.*

The results of the mesh-dependence study are shown in Figure 2.4. Mesh sensitivity was evaluated using three models: (a) a tetrahedral mesh with 3 million cells, (c) a hexahedral mesh with 5 million cells, and (e) a hexahedral mesh with 9 million cells. For this comparison, the inlet boundary condition (time-varying flow rate) was taken from the input waveform in Figure 2.3, and the flow fields at t = 0.036[s] were examined. The vorticity iso-surface at ω= 0.03 was chosen such that well-developed vortex rings were present in the solution for cases (e) and (f).

As shown in Figure 2.4(b), the 3-million-cell mesh yields a velocity field that appears smeared, indicating insufficient spatial resolution; moreover, vortical structures are visible only inside the orifice. In contrast, Figure 2.4(d) demonstrates that the 5-million-cell mesh

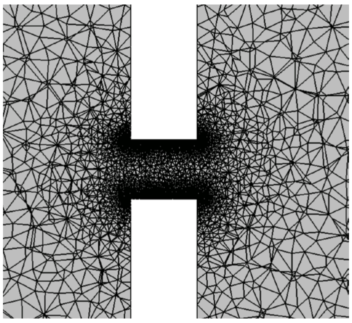

(a) Cross-sectional view of the 3-million-cell tetrahedral mesh

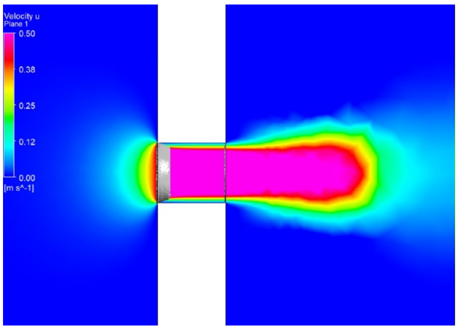

(b) Velocity contour plot and vorticity iso-surface at ω = 0.03 for the 3-million-cell tetrahedral mesh

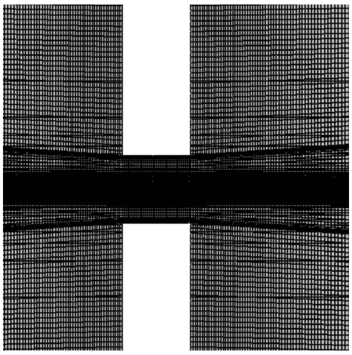

(c) Cross-sectional view of the 5-million-cell hexahedral mesh

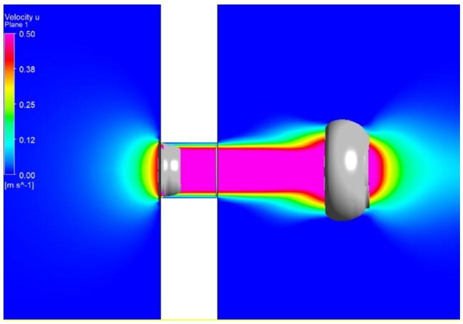

(d) Velocity contour plot and vorticity iso-surface at ω = 0.03 for the 5-million-cell hexahedral mesh

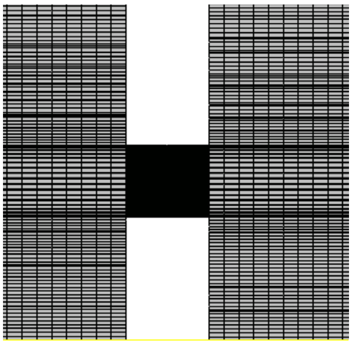

(e) Cross-sectional view of the 9-million-cell hexahedral mesh

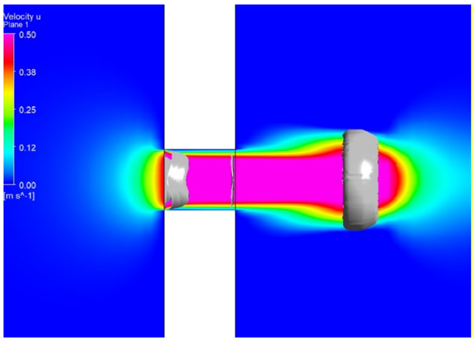

(f) Velocity contour plot and vorticity iso-surface at ω = 0.03 for the 9-million-cell hexahedral mesh

Figure 2.4 Comparison of results as grid independence verification

provides improved spatial resolution, with sharp velocity gradients and vortices captured not only within the orifice but also in regions where the velocity attains its maximum. As shown in Figure 2.4(f), further increasing the mesh size to 9 million cells results in essentially the same flow structures and velocity distributions as those obtained with the 5-million-cell mesh in Figure 2.4(d). Based on these results, a mesh with 5 million cells was adopted for all subsequent simulations. In this mesh, 38 cells are distributed in the radial direction within the orifice, and the first cell height at the wall is approximately 2[μm]. The detailed mesh configuration is shown in Figure 2.5.

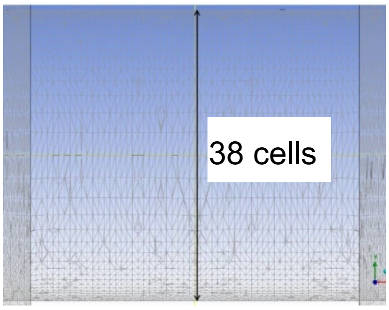

Figure 2.5 Analysis grid of the orifice area

3. Analysis Results

3.1 Unidirectional Flow

The inlet condition is a rectangular waveform as shown in Figure 2.2, and the discussion here focuses on the flow corresponding to the nonzero mass flow rate of 0.0001[kg/s] in the interval t = 0.03 – 0.05 [s], following the zero-flow interval t = 0.01 – 0.03 [s].
Time-series distributions of vorticity contours, velocity vectors in the x-direction, and the Q-criterion are presented for each phase, and the vortex structures and flow patterns are compared on this basis. Here, the x-direction velocity is defined as positive for flow from left to right in the Figures. The vorticity field is visualized over the range 0–5000, and regions with Q values greater than 1×10^7 are used to identify vortex cores.
The Q-criterion is an objective measure for defining and extracting vortical structures in a flow field. By visualizing iso-surfaces of positive Q, where local rotation dominates over strain (deformation), the growth and decay of vortex rings can be clearly captured. Mathematically, Q is defined using the second invariant of the velocity-gradient tensor as

$$Q = \frac{1}{2}\left(\Omega_{ij} \cdot \Omega_{ij} - S_{ij} \cdot S_{ij}\right) \tag{3}$$

where Ω_{ij} is the rotation tensor (rotational component of the flow), and S_{ij} is the strain-rate tensor (shear and deformational component of the flow).

3.1.1 Periodic Vortex Generation

In this section, the periodic vortex-generation process under forward-flow conditions is organized and discussed along the time sequence (a)–(h), based on vorticity contours, streamwise x-direction velocity vectors, and Q-criterion fields obtained from the CFD analysis. Figure 3.1.1 shows the temporal evolution of these three quantities in the vicinity of the orifice for the forward-flow case. In frame (a), the fluid begins to accelerate in the positive (rightward) direction. Upstream of the orifice, viscous friction at the inner wall decelerates the fluid adjacent to the wall, and a boundary layer with a wall-normal velocity gradient form and develops. Within this boundary layer, vorticity is continuously generated and accumulated at the wall due to the velocity difference between the core flow and the near-wall region and is transported downstream while remaining attached to the wall from

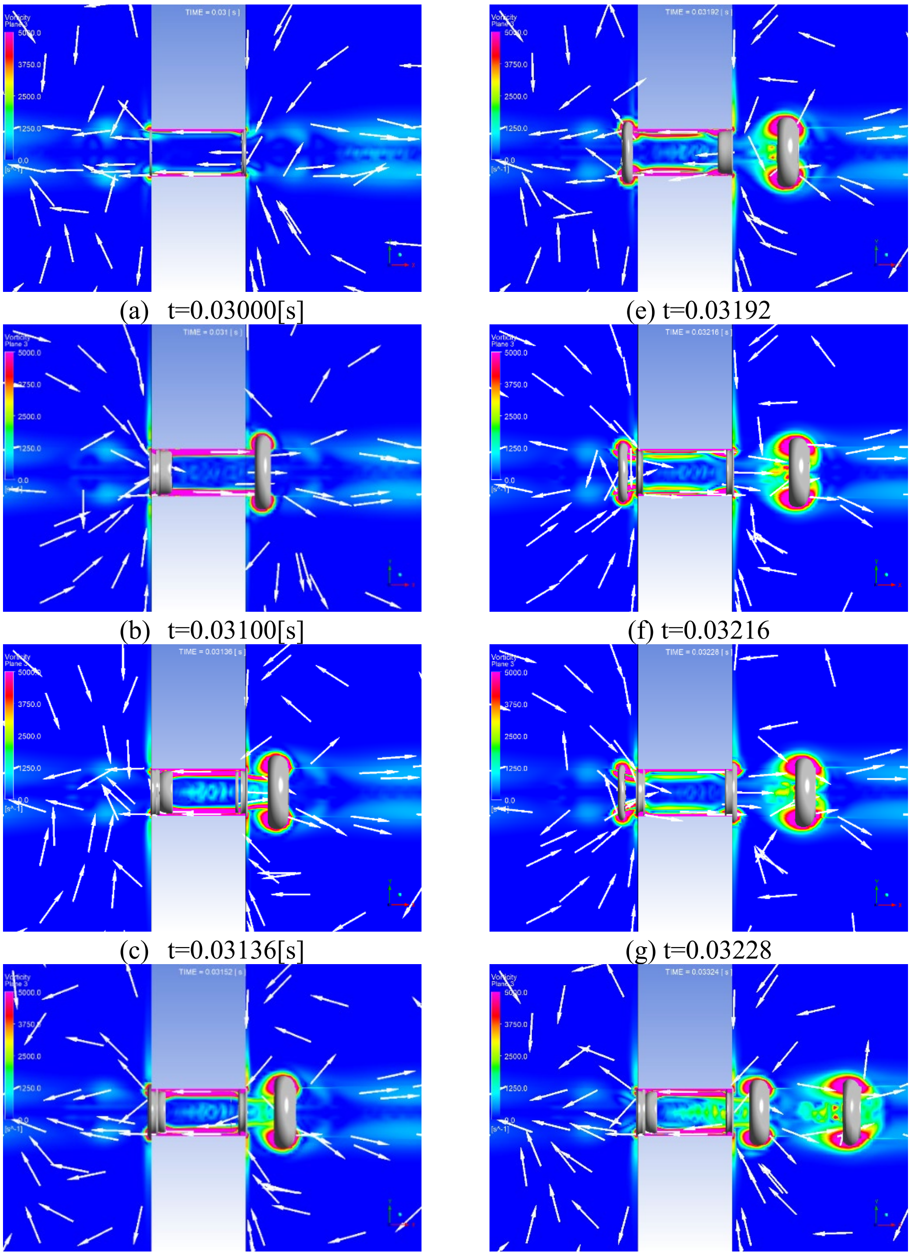

(a) t=0.03000[s]
(e) t=0.03192
(b) t=0.03100[s]
(f) t=0.03216
(c) t=0.03136[s]
(g) t=0.03228
(d) t=0.03152[s]
(h) t=0.03324

Figure 3.1.1 Vorticity contour, velocity vectors, Q-criterion for unidirectional flow (Q=const.)

the orifice inlet to the outlet. In addition, a small vortex ring is formed at the orifice inlet (left side) due to slight flow separation that occurs as the flow turns around the inlet corner into the orifice. In frame (b), when the boundary layer reaches the vicinity of the orifice exit edge, it separates from the wall under the adverse pressure gradient induced by the sudden expansion of the flow passage, thereby forming a free shear layer. This shear layer then rolls up under itself-induced velocity and generates a starting vortex ring at the orifice exit edge. The starting vortex thus formed produces an induced velocity field associated with its circulation, giving rise to a vortical structure that carries a reverse flow relative to the mainstream in the vicinity of the orifice exit edge. In frames (c) and (d), as the starting vortex is gradually transported downstream by the mainstream, it strongly interacts with the reverse-flow vortical structure near the exit edge, generating a large velocity shear along their interface. This shear causes part of the vortex to be cut off and split along the streamwise direction, which can be clearly observed in the flow field. In frame (e), prior to fragmentation, the reverse flow induced by the starting vortex would nominally tend to enter the orifice interior, but such inflow is suppressed by the downstream-directed mainstream. At the moment when the starting vortex is fragmented, the vortical mass remaining on the upstream side exhibits a transient motion opposite to the mainstream due to inertia, leading to a localized backflow near the orifice inlet. As a result, a new vortex ring (hereafter referred to as the secondary vortex ring) is formed in the vicinity of the orifice inlet edge. In frames (f), (g), and (h), the secondary vortex generated near the inlet edge is rapidly diffused and attenuated as it is transported downstream through interaction with the mainstream and eventually dissipates. Concomitant with the dissipation of the secondary vortex ring, vorticity is again generated on the inner wall of the orifice due to the renewed velocity difference between the mainstream and the near-wall region, and the streamwise boundary-layer structure along the inner diameter wall is re-established. Subsequently, the same sequence of events—(a) boundary-layer development, (b) roll-up of the free shear layer and generation of a starting vortex, (c)(d) fragmentation of the starting vortex by its induced flow, (e) generation of a secondary vortex ring near the inlet, and (f)(g)(h) dissipation of the secondary vortex ring and reconstruction of the boundary layer—is repeated in time, thereby sustaining periodic vortex-ring generation at the orifice exit.

From the above, the present CFD analysis qualitatively demonstrates that periodic vortex generation in forward orifice flow is governed by the series of unsteady phenomena described in (a)–(h). This vortex-generation mechanism shows good qualitative agreement with the vortex-ring formation process reported in the visualization experiments of Pullin et al. [16]. In this case, vortex rings are transported downstream at time intervals of Δt=0.0017[s]. This interval depends, among other factors, on the magnitude of viscous resistance associated with the orifice length.

3.1.2 Stopping Vortex Generation

In this section, the vortex-formation process that occurs when the inlet flow rate is stepped to zero at t = 0.01[s] from a forward-flow state is examined along the time sequence (a)–(h), based on vorticity contours obtained from the CFD analysis. Figure 3.1.2 shows the temporal evolution of the vorticity distribution in the vicinity of the orifice. In frame (a), the inlet mass flow rate is held constant at 0.0001[kg/s], and the periodic vortex-generation cycle described in Figure 3.1.1(a)–(h) is still ongoing. At this stage, the free shear layer separated from the orifice exit edge rolls up and forms a starting vortex at the exit edge.

In frame (b), the influence of the abrupt reduction in inlet flow rate at Δt=0.01[s] has not yet become pronounced. The starting vortex that has formed begins, through its own induced velocity field, to generate a region of reverse flow relative to the mainstream in the vicinity of the orifice exit edge. In frame (c), the effect of the stepwise reduction of the inlet flow rate at t = 0.01[s] starts to appear. The fluid mass inside the orifice and near the exit, excluding the near-wall region, continues to move downstream due to inertia, whereas

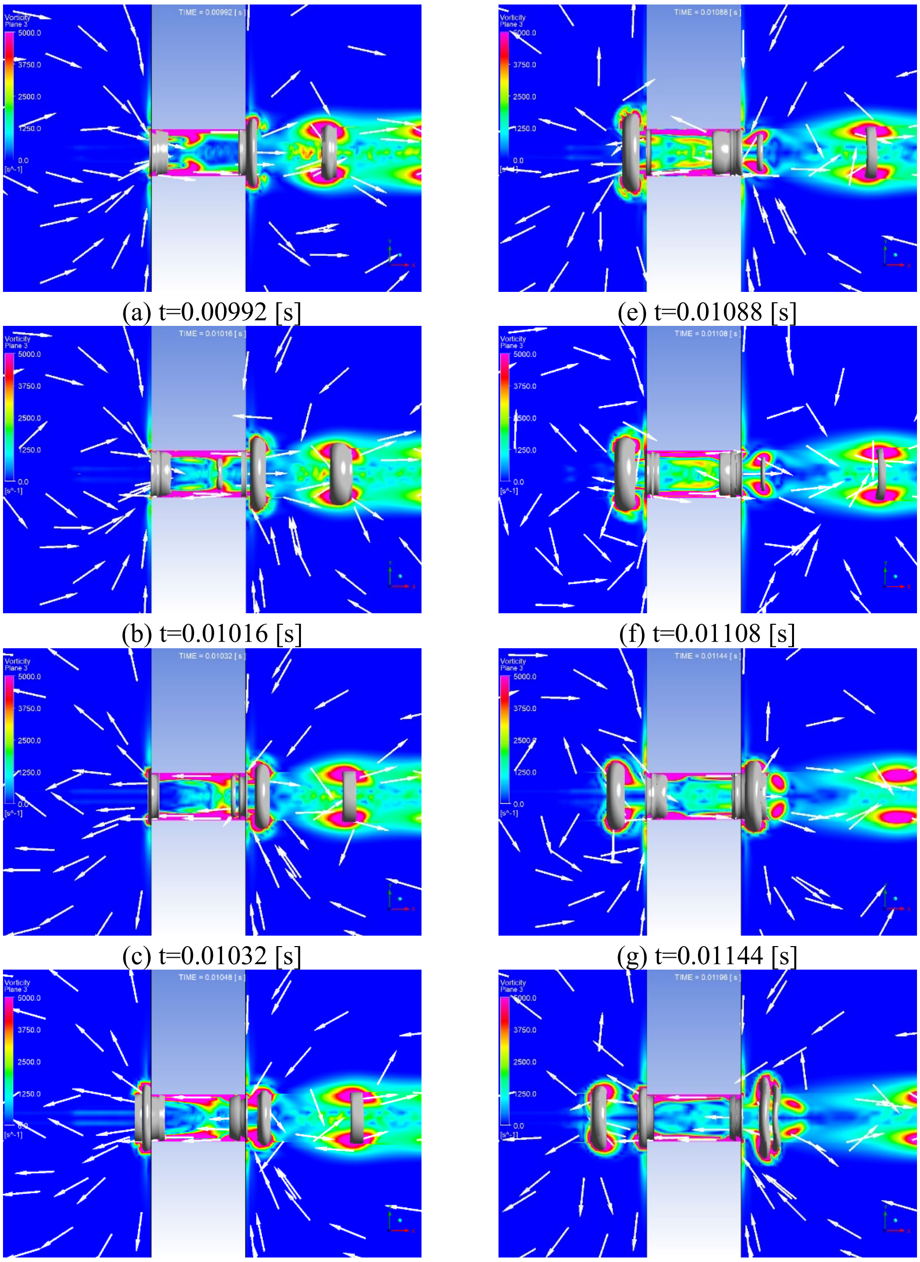

(a) t=0.00992 [s] (e) t=0.01088 [s]
(b) t=0.01016 [s] (f) t=0.01108 [s]
(c) t=0.01032 [s] (g) t=0.01144 [s]
(d) t=0.01048 [s] (h) t=0.01196 [s]

Figure 3.1.2 Vorticity contour, velocity vectors, Q-criterion for unidirectional flow (step flow rate drop to zero at t=0.01[s])

the flow at the orifice exit edge is pulled back toward the orifice interior as the mainstream decelerates. This backflow, together with the induced velocity field of the pre-existing starting vortex, generates a new vortex ring of opposite sign immediately downstream of the orifice exit edge. This structure is referred to as a stopping vortex. It is found to be in qualitative agreement with the stopping vortex reported in the visualization experiments of Pullin et al. [16]. In frame (d), the starting vortex located at the orifice exit edge is subjected to strong shear in the vicinity of the exit edge due to the combined action of the stopping vortex and the mainstream and is consequently split. The fragmented vortex mass, influenced by the stopping vortex and by fluid inertia at the moment of fragmentation, exhibits a transient motion opposite to the mainstream, thereby giving rise to a new vortex ring of opposite sense to the mainstream at the orifice inlet edge. In frame (e), the transient reverse flow directed into the orifice interior leads to growth of the vortex ring at the inlet edge and simultaneously draws the vortex mass remaining on the outlet side back toward the interior of the orifice. In frame (f), similarly to frame (c), the reversal of the main-flow direction causes the flow near the orifice to be redirected downstream. As a result, a stopping vortex of opposite sign to the inlet-edge vortex ring is generated just downstream of the inlet edge. At the same time, the vortex mass that remained on the outlet side is pushed further downstream by the mainstream. In frame (g), the inlet-side vortex ring is again subjected to strong shear and is fragmented due to fluid inertia associated with the change in flow direction toward the downstream side and due to its interaction with the stopping vortex. Simultaneously, a new vortex ring is formed at the orifice exit edge, and the vortex masses that remained in the outlet opening and within the orifice bore are transported downstream by the mainstream. In frame (h), the change in the main-flow direction causes the vortex ring on the outlet side to be fragmented, while a new vortex ring is generated on the inlet side. Although vorticity continues to be generated periodically from the shear layer, the absence of external flow-rate supply leads to an overall reduction in the vorticity level, and the vortical structures are markedly attenuated. Thus, immediately after the abrupt reduction in flow rate, repeated generation and subsequent fragmentation of vortex rings at the orifice inlet and exit edges occur through the splitting of the starting vortex and the subsequent formation of stopping vortices. The present CFD analysis confirms that this process ultimately converges to a vorticity-dissipation regime dominated by viscous diffusion.

3.1. Alternative Flow

In this section, the flow field around the orifice under alternating-flow conditions is examined by comparing vortex structures and flow patterns using streamwise x-direction velocity contours, velocity vectors, streamlines, and Q-criterion distributions.

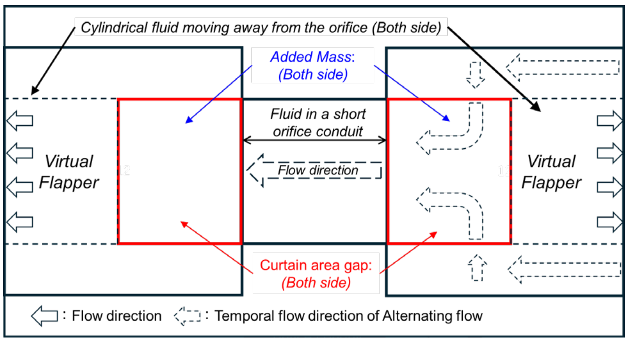

Figure 3.2.1 Simplified flow pattern near an orifice

From the flow patterns discussed in the previous section, it was found that the upstream and downstream flow fields have a significant influence on the dynamic characteristics of the flow within the orifice. Accordingly, two characteristic regions are identified upstream and downstream of the orifice, as shown in Figure 3.2.1 (hereafter referred to as the "virtual flapper" region and the "virtual curtain" region). These regions are considered to affect, among other properties, the added mass associated with the internal orifice flow. In what follows, the detailed flow patterns within these regions under alternating-flow conditions are analysed.

3.2.1 Flow patterns (200[Hz])

Figure 3.2.2 shows the correspondence between time in the input flow-rate waveform at 200 [Hz] and the phases (a)–(h) (which match the Figure labels).

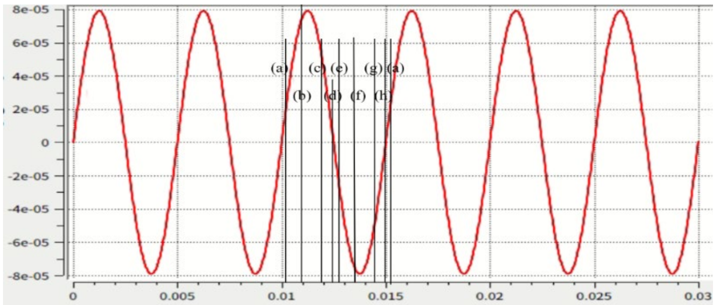

Figure 3.2.2 Correspondence between time history of input waveform and phase labels

Figure 3.2.3 presents the time-series distributions of streamwise x-direction velocity contours, velocity vectors, and Q-criterion for each phase (a)–(h) within one cycle at 200 [Hz]. Here, the x-direction velocity is defined as positive for flow from left to right in the Figures, and the velocity contours are visualized within the range ±0.2 [m/s]. The vortex-core regions are visualized using Q values greater than $2×10^6$ for the 200 [Hz] case. A total of six cycles were computed, and the data shown are taken from after the second cycle, when the flow field was judged to have reached a periodically steady state.

At phase (a), the main flow, which in the first half-cycle had been directed from the right chamber to the left chamber, switches direction and a flow from the left chamber to the right chamber begins to develop. In the central region of the orifice bore, a low-velocity region forms in association with this flow-reversal process, and a fully developed jet has not yet been established. Near the inlet orifice edge (left side), the Virtual Flapper region, a small-scale reverse-flow zone that remains due to inertia from the previous half-cycle, persists. The main flow circumvents this reverse-flow region by passing around its outer periphery and enters the orifice with a slight contraction at the inlet (left side), where a vortex ring is formed. This constitutes the Virtual Curtain region. On the other hand, near the outlet orifice edge (right side), a shear layer corresponding to the new main-flow direction begins to form, and a starting vortex is generated in association with this shear layer.

At phase (b), the main flow from the left chamber to the right chamber further intensifies, and the x-direction velocity in the central region of the orifice bore attains an almost uniform positive value in the streamwise direction. The vortex ring that was generated at the orifice inlet edge (left side) in phase (a) grows significantly under the influence of the increasing main-flow velocity. At the orifice exit edge (right side), the roll-up of the shear layer associated with the new main-flow direction progresses, and the vortex ring corresponding to the starting vortex for the rightward flow develops downstream. At phase (c), although the main flow from the left chamber to the right chamber has just passed the peak flow-rate

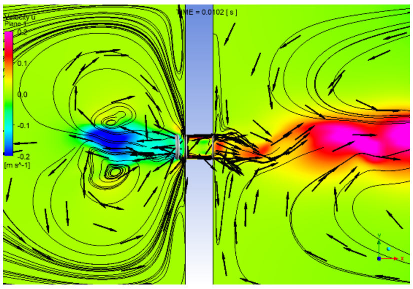

Phase (a); main flow directed to the right

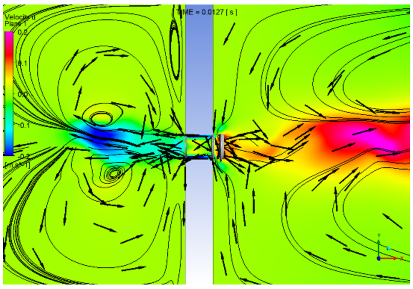

Phase (e); main flow directed to the left

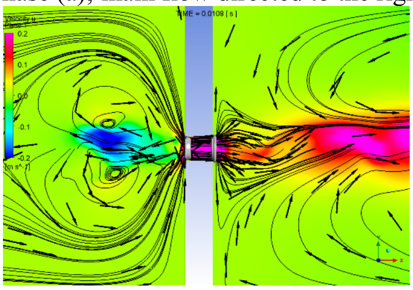

Phase (b); main flow directed to the right

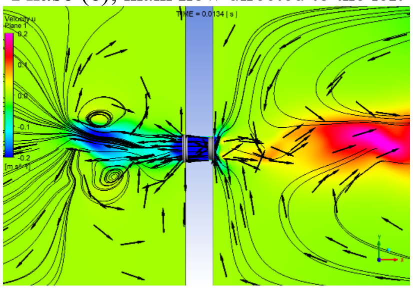

Phase (f); main flow directed to the left

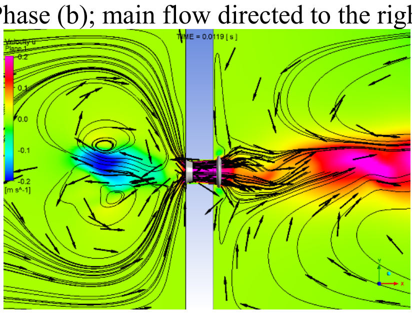

Phase (c); main flow directed to the right

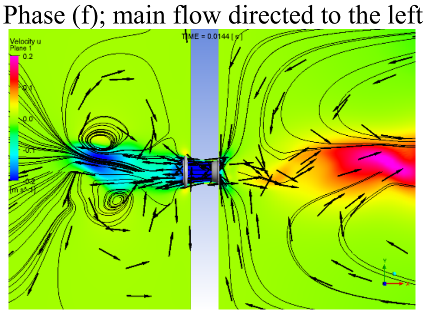

Phase (g); main flow directed to the left

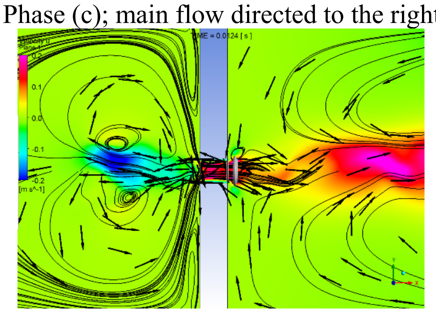

Phase (d); main flow directed to the right

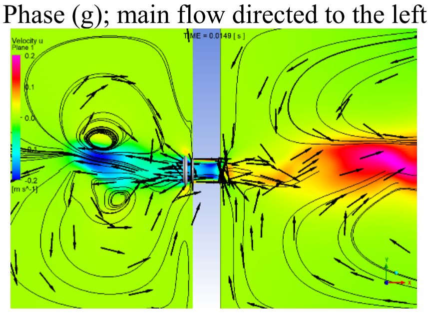

Phase (h); main flow directed to the left

Figure 3.2.3 Velocity contours, vectors, streamlines & Q-criterion iso-surface for 200[Hz] alternating flow

amplitude occurring near phase (b), the x-direction velocity in the central region of the orifice bore still exhibits an almost uniform positive value in the streamwise direction, and a jet-like flow is established. At the orifice exit edge (right side), the starting vortex associated with the rightward flow grows further downstream, and the region of concentrated vorticity expands into the right chamber. At phase (d), the main flow from the left chamber to the right chamber is in the stage just before reversing direction. The x-direction velocity in the central region of the orifice bore maintains a positive component but decreases markedly, and the flow rate approaches its minimum. The vortex ring that has developed near the orifice inlet edge (left side) decays under the influence of the decelerating main flow. In contrast, the fluid mass in the central region of the orifice and near the exit continues to be carried downstream (to the right) by inertia, while at the orifice exit edge the deceleration of the main flow induces a reverse flow along the wall toward the upstream side (left). The interaction between this reverse flow and the induced velocity field of the pre-existing starting vortex leads to the formation of a stopping vortex ring near the orifice exit edge (right side), which rotates in the opposite sense to the starting vortex associated with the rightward flow. At phase (e), the main-flow direction begins to reverse from left-to-right to right-to-left, i.e., from the left chamber toward the right chamber to the right chamber toward the left chamber. Inside the orifice, a low-velocity reverse-flow region persists in the central part, while a leftward flow has already developed near the wall. As time progresses, the overall flow field transitions to a quasi-uniform right-to-left stream. The vortex ring formed near the orifice exit edge (right side) up to the preceding phase (d) decays and is simultaneously split, resulting in two vortical structures, one at the orifice exit edge on the left side and one on the right side. At the orifice exit edge on the left side, which now acts as the outlet for the new (leftward) main-flow direction, roll-up of the wall-bounded shear layer induced by the reversed main flow advances; consequently, the left-side vortex ring aligned with the right-to-left flow is generated and grows. The right-side vortex ring, together with the residual reverse-flow region (Virtual Flapper), decays under the influence of the leftward main flow. From phase (e) to phase (h), the main-flow direction is fully reversed, and a flow from the right chamber to the left chamber is established. The distribution of the velocity contours exhibits a nearly mirror-symmetric pattern relative to phases (a)–(d), reflecting the flow-direction reversal. A Virtual Flapper region, characterized by a reverse-flow zone opposite to the main (leftward) stream, appears near the orifice inlet (right side), and a Virtual Curtain region is formed in which the main flow bypasses this reverse-flow zone, entering the orifice from the outer periphery toward the center.

3.2.2 Flow patterns (1500[Hz])

Figure 3.2.4 shows the correspondence between time in the input flow-rate waveform at 1500 [Hz] and the phases (a)–(h) (which match the Figure labels).
Figure 3.2.5 presents the time-series distributions of streamwise x-direction velocity contours, velocity vectors, and Q-criterion for each phase (a)–(h) within one cycle at 1500 [Hz]. Here, the x-direction velocity is defined as positive for flow from left to right in the Figures, and the velocity contours are visualized within the range ±0.2 [m/s]. For the 1500 [Hz] case, vortex-core regions are visualized using Q values greater than 1×10^7. In all cases, the data are taken from simulations after 30 cycles, at which point the flow field was judged to have reached a periodically steady state.
At phase (a), the main-flow direction switches from that of the preceding half-cycle, and the flow begins to enter from the left chamber into the right chamber. At this time, a new starting vortex is observed to form near the orifice exit edge (right side). In the central region of the orifice, excluding the near-wall region, a low-velocity zone remains, and the flow field is in transition from a nearly uniform reverse-flow state to a nearly uniform main-flow state. In

the vicinity of the orifice inlet edge (left side), a reverse-flow region (Virtual Flapper region) persists, in which the flow from the previous half-cycle is retained due to fluid inertia. The main flow bypasses this Virtual Flapper region by passing around its periphery and enters

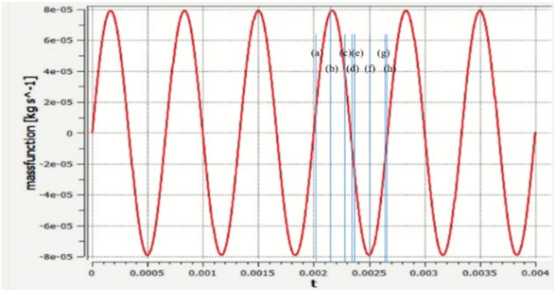

Figure 3.2.4 Correspondence between time history of input waveform and phase numbers

the orifice with a contracted cross-section at the inlet (left side), forming a Virtual Curtain region. Near the orifice inlet edge (left side), the inflow from the outer periphery of this Virtual Curtain region and the residual reverse-flow region (Virtual Flapper region) together give rise to the formation of a new vortex ring. At phase (b), the main flow from the left chamber to the right chamber is further intensified, and a jet-like flow with an almost uniform streamwise velocity is established inside the orifice. The vortex ring that formed near the orifice inlet edge (left side) in phase (a) grows significantly due to the increased inflow velocity along the outer periphery of the Virtual Curtain region. Meanwhile, at the orifice exit edge (right side), the starting vortex generated by the roll-up of the shear layer further develops in the downstream direction and appears as a strong concentration of vorticity around the jet. At phase (c), although the main flow from the left chamber to the right chamber has just passed the maximum flow-rate amplitude occurring near phase (b), the x-direction velocity in the orifice-bore region still maintains an almost uniform distribution in the streamwise direction, and a strong jet is sustained. At the orifice inlet edge (left side), the shear layer formed up to the previous phase continues to grow downstream, whereas at the orifice exit edge (right side), the starting vortex ring begins to decay. At phase (d), the main flow that has been directed from the left chamber to the right chamber up to the preceding phase weakens, and the flow is in the process of reversing from right to left. The fluid mass in the central region of the orifice and near the orifice exit (right side), which constitutes a Virtual Flapper region, still tends to move toward the downstream side of the right chamber due to inertia from its prior motion. In contrast, near the orifice exit edge (right side), deceleration of the main flow induces a reverse (leftward) flow along the inner-wall surface of the orifice. The strong shear arising from the interaction between this reverse flow and the induced velocity field of the starting vortex leads to the formation of a stopping vortex, which rotates in the opposite sense to the starting vortex, near the orifice exit edge (right side). The vortex ring that existed near the orifice inlet edge (left side) in phase (c) is still present, although it is attenuating. At phase (e), the main-flow direction has completely reversed, and the flow now proceeds from the right chamber toward the left chamber. A low-velocity region remains in the central part of the orifice, but the near-wall region has already started to accelerate, and the flow field is transitioning toward a nearly uniform main-flow field in the new (leftward) direction. Meanwhile, up to the preceding phase (d), a Virtual Curtain region has formed near the right orifice edge from a locally stagnated state, and a reverse-flow region (Virtual Flapper) persists downstream of it. From

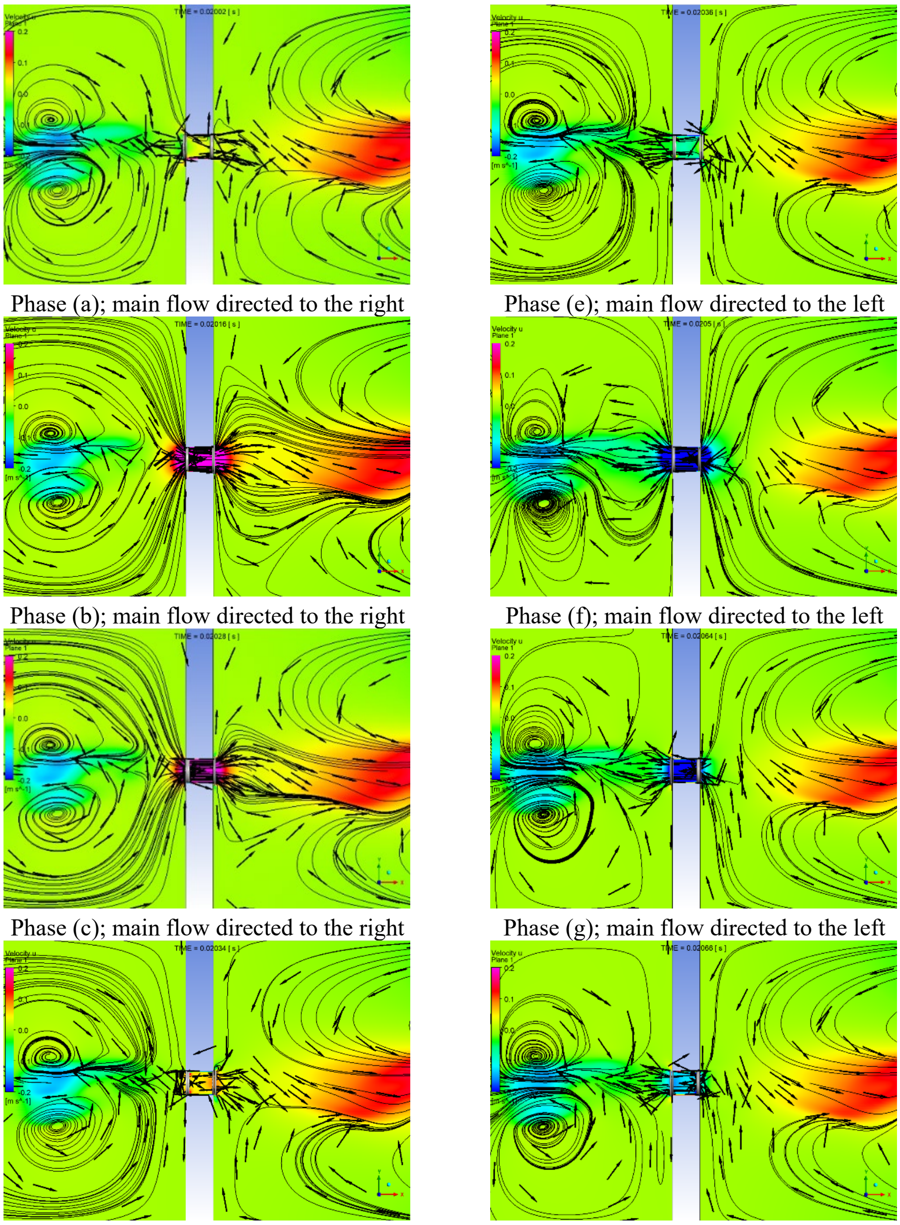

Phase (a); main flow directed to the right
Phase (e); main flow directed to the left
Phase (b); main flow directed to the right
Phase (f); main flow directed to the left
Phase (c); main flow directed to the right
Phase (g); main flow directed to the left
Phase (d); main flow directed to the right
Phase (h); main flow directed to the left

Figure 3.2.5 Velocity contour & Q-criterion iso-surface for 1500[Hz] alternating flow

phases (e) to (h), the main-flow direction remains reversed, and a flow from the right chamber to the left chamber is established. The distributions of the velocity contours exhibit patterns that are nearly mirror images of those in phases (a)–(d), reflecting the reversal of the flow direction. A Virtual Flapper region, characterized by a reverse-flow zone opposite to the main (leftward) stream, appears near the right orifice, while a Virtual Curtain region forms in which the main flow avoids this reverse-flow zone and enters from the outer periphery toward the orifice center.

3.2.3 Comparison of Flow Patterns (200 V.S. 1500 [Hz])

Under the 200 [Hz] condition, each half-cycle is sufficiently long that the velocity distribution inside the orifice becomes nearly uniform at an early stage. As a result, the starting vortex, stopping vortex, and the reverse-flow Virtual Flapper and Virtual Curtain regions are relatively weak, and the entire system undergoes a quasi-steady reciprocating motion as a single entity.

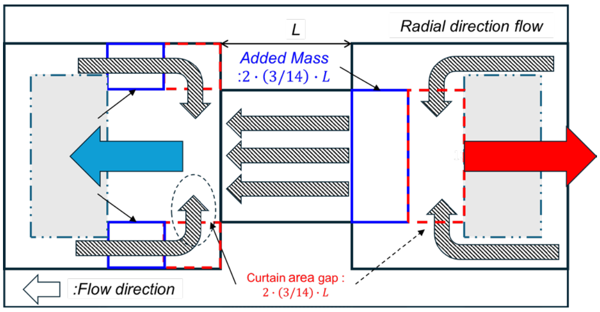

(a) Schematic of the flow field when the flow is directed from right to left

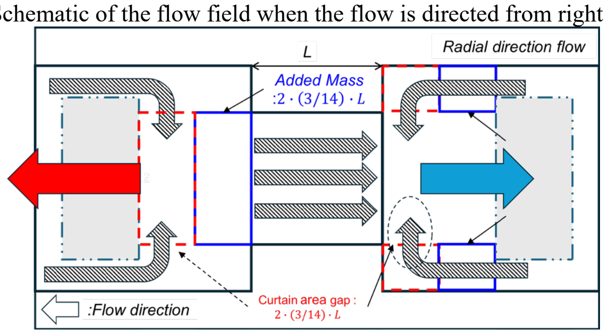

(b) Schematic of the flow field when the flow is directed from left to right

Figure 3.2.6 Existence of Virtual Flapper and Virtual Curtain regions with a well-defined flow direction

By contrast, under the 1500 [Hz] condition, the switching of the main flow does not fully propagate across the entire orifice cross-section, and the Virtual Flapper and Virtual Curtain regions at the orifice inlet, as well as the starting and stopping vortices on the outlet side, remain strongly developed. Consequently, throughout phases (a)–(d), a strongly non-uniform and highly unsteady flow field is formed, characterized by pronounced velocity gradients and vortical structures. Phases (e)–(h) exhibit flow-direction-reversed patterns that are nearly mirror images of phases (a)–(d), and the same tendencies are observed. From these results, the existence of Virtual Flapper and Virtual Curtain regions with a fixed flow direction, as illustrated in Figure 3.2.6, has been confirmed. It has been clarified that changes in the flow velocity within these regions significantly affect the fluid inertia in the vicinity of the orifice.

4. Effective Inertial Length in Alternating Orifice Flow

In this section, the effective inertial length in oscillatory orifice flow is discussed based on the numerical results for the 200 [Hz] and 1500 [Hz] cases. As is evident from the time-series results in Figure 3.2.3 and 3.2.5, the Virtual Flapper and Virtual Curtain regions are periodically formed and disappear on both sides of the orifice in synchrony with the acceleration and deceleration of the main flow. These structures constitute a continuous velocity field with the fluid column inside the orifice, indicating that not only the fluid within the orifice, but also the fluid in the upstream and downstream chambers, is accelerated and decelerated as a single system. This implies an inertial effect equivalent to an apparent extension of the orifice length. In other words, the presence of the Virtual Flapper and Virtual Curtain regions and their associated added-mass effect can be interpreted as imparting, in addition to the geometric orifice length, an extended region near the orifice end faces (here referred to as the effective inertial length). Inspection of the velocity-contour fields in Figure 3.2.3 and 3.2.5 shows that, for both 200 [Hz] and 1500 [Hz], reverse-flow zones and quasi-cylindrical velocity-distribution regions are formed over several millimetres in the vicinity of the orifice openings. Because these regions are periodically accelerated and decelerated together with the main flow, the effective inertial length exceeds the geometric length by a substantial margin. Focusing on the frequency dependence, under the 200 [Hz] condition each half-cycle is sufficiently long that the Virtual Flapper and Virtual Curtain regions remain relatively weak, and the velocity distribution within the chambers is smoothed over time. As a result, the region corresponding to the extended length of the orifice fluid column is confined to the immediate vicinity of the orifice, and the increase in effective inertial length is considered to be relatively moderate compared with the geometric length. In contrast, under the 1500 [Hz] condition, the flow-direction reversal proceeds to the next half-cycle before it has fully propagated across the entire orifice cross-section. Consequently, the Virtual Flapper and Virtual Curtain regions persist strongly across phases, and a broad additional liquid-column region is maintained in the upstream and downstream chambers. The fluid volume that is effectively coupled to the orifice fluid column is therefore larger than in the 200 [Hz] case, and the effective orifice length greatly exceeds the geometric length, with a tendency to increase further as the oscillation frequency increases. These findings demonstrate that, in oscillatory orifice flow, an inertia assessment based solely on the geometric orifice length is inadequate. Introducing an effective inertial length that incorporates the Virtual Flapper and Virtual Curtain regions and their associated added-mass effects is essential for correctly describing the damping characteristics of oscillatory flow through an orifice. It should be noted, however, that the present analysis focuses on a local region in the vicinity of the orifice and does not evaluate the momentum balance for the entire system, including the full chamber volumes. Accordingly, the spatial extent of the Virtual Flapper and Virtual Curtain regions is not necessarily captured completely, and some uncertainty remains in the quantitative evaluation of the effective inertial length.

5. Conclusions

In this study, CFD analysis was used to clarify the processes of periodic vortex generation and stopping-vortex formation in unidirectional orifice flow, and to qualitatively investigate new features specific to alternating orifice flow, namely the Virtual Flapper flow, the Virtual Curtain region, and their associated added-mass effects. The main findings are as follows.

5.1 Unidirectional Flow

It was confirmed that the vortical structures around the orifice are composed of the following sequence of unsteady processes:

- vorticity generation within the boundary layer along the inner wall of the orifice
- formation of a starting vortex due to roll-up of the free shear layer at the orifice exit edge
- generation of a stopping vortex through the interaction between the induced flow of the starting vortex and the mainstream, and the resulting fragmentation of the starting vortex
- generation of secondary vortex rings in the vicinity of the orifice inlet
- downstream transport and dissipation of the secondary vortex rings, accompanied by reconstruction of the boundary-layer structure.

It was also confirmed that this near-orifice region (corresponding to the Virtual Curtain region) plays an important role in the flow dynamics.

5.2 Alternative Flow

Under alternating Flow conditions, a flow composed of the Virtual Flapper region and the Virtual Curtain region exists in a fixed spatial arrangement around the orifice and exhibits periodic strengthening and weakening. The flow inside the orifice reverses its direction in synchrony with the acceleration and deceleration of the mainstream. Within the Virtual Curtain region, a spatially fixed flow is continuously formed from the outer-diameter side toward the inner-diameter side on both sides of the orifice, while its intensity varies in time. Due to the Virtual Flapper and Virtual Curtain regions and their associated added mass, additional liquid-column regions are generated upstream and downstream of the orifice, and the effective inertial length greatly exceeds the geometric orifice length. Therefore, when evaluating the damping characteristics of alternating flow through an orifice, it is necessary to consider not only the geometric orifice length but also the effective inertial length.

References

[1] Johansen, F. C. : Flow through Pipe Orifices at Low Reynolds Numbers, A.M. I. Mech. E., p.231-245 (1929).

[2] A. F. D'Souza, R. Oldenburger, Dynamic Response of Fluid Lines, Journal of Basic Engineering, p.589-598(1969).

[3] Benjamin,E. W.,Victor,L.S.: Fluid Transient in Systems, PRENTICE HALL, p. 2-9 (1993).

[4] Lau, K. K., Edge, K.A. and Johnston, D.: Impedance Characteristics of Hydraulic Orifices, Proc. Instn. Mech. Engrs, Part I: J. Sys. Control Eng. 209. p.241-253 (1995).

[5] D. Nigel Johnston: Prediction of Fluid Inertance in Nonuniform Passageways, Journal of Fluids Engineering, Vol. 128, No.2, p.266-275 (2006).

[6] Higo,H., Tanaka K., Yamaguchi,T.: New One Dimensional Modeling for Complex Oil Passage Coupled with CFD Results, Proceedings of the ASME/BATH 2014 Symposium on Fluid Power & Motion Control FPMC2014, 2014.

[7] Uchida,S.: The Pulsating Viscous Flow Superposed on the Steady Laminar Motion of Incompressible Fluid in a Circular Pipe, ZAMP Vol.7, p.403-422 (1956).

[8] Munekazu, O., Manabu, I., Tateo,Usui.: Flow Pattern and Frictional Losses in Pulsating Pipe Flow, Part5, Wall Shear Stress and Flow Pattern in a Laminar Flow, Bulletin of the JSME, Vol. 24, No.187, p.75-81 (1981).

[9] S. Masuda, et. al., 'Modelling and simulation of damping orifices for pressure control valves, Proc. ISFP 2024 JFPS, 1A2-03, https://doi.org/10.5739/jfps.52.8
[10] Rosenberg, R.C. and Karnopp,D.C.: Introduction to Physical System Dynamics, McGraw-Hill, 1983.
[11] Seiei Masuda, et. al., 'Modelling and Simulation of Damping Orifices for Pressure Control Valves 2nd Report), Proceedings of the 15th International Fluid Power Conference (15th IFK), 9–11 March 2026.
[12] S. Oshima, et. al., 'Frequency Characteristics of Cylindrical Short Chokes for Hydraulic Valves (In case of using general hydraulic oil), J. Hydraulics. Pneumatics (in Japanese), Vol.15, No.2, 1984, pp.157-165,
[13] S. Miyagawa, 'Frequency Characteristics of Cylindrical Short Chokes, J. JSME (in Japanese), Vol.42, No.355, 1971, pp.847-856, https://doi.org/10.1299/kikai1938.42.847
[14] Catherine Loudon, et. al., 'The Use of the Dimensionless Womersley Number to Characterize the Unsteady Nature of Internal Flow, Journal of Theoretical Biology, vol. 191, No.1, 1998, doi:10.1006/jtbi.1997.0564
[15] J. R. Womersley, 'An elastic tube theory of pulse transmission and oscillatory flow in mammalian arteries, WADC Technical Report 56-614, Wright Air Development Center, Wright-Patterson AFB, OH, USA, Jan. 1957.
[16] M. Van Dyke, 'An Album of Fluid Motion, The Parabolic Press, Stanford, CA, 1982.
[17] ANSYS: CFX-Pre User's Guide Release 2025R1 (2025)

NOMENCLATURE

Symbol	Explanation of variable symbols
A_R	Metering valve opening area
P_1	Inlet pressure of metering valve
P_2	Outlet pressure of metering valve
P_{2S}	Pressure of Spring room
P_C	Pressure downstream of Pressure Control valve
Q	Q-criterion
Q_0	Flow rate through damping orifice
Q_{By}	Bypass flow rate through differential pressure control valve
Q_{MV}	Flow rate through metering valve
Q_P	Pump flow rate
S_{ij}	Shear and deformational component of the flow
t	Time
x	Cartesian coordinate in the orifice streamwise direction
X	Valve displacement
W_O	Womersley number
ω	Vorticity
Ω_{ij}	rotational component of the flow